Imaging performance of a DEPFET pixel Bioscope system in Tritium autoradiography

J. Ulrici[a,*,1], P. Fischer[a,2], P. Klein[b,3], G. Lutz[b], W. Neeser[a,4], R. Richter[b], L. Strüder[b], M. Trimpl[a], N. Wermes[a]

[a]*Physikalisches Institut der Universität Bonn, Nußallee 12, D-53115 Bonn, Germany*
[b]*MPI Halbleiterlabor, Otto-Hahn-Ring 6, D-81739 München, Germany*

Abstract

A Bioscope system based on a 64×64-matrix of DEPFET pixels has been developed for real-time digital autoradiography in biomedical applications. It provides very good energy and spatial resolution at the same time. The DEPFET pixel cells consist of *p*-channel JFETs integrated into the high-ohmic *n*-silicon substrate. This leads to a very low noise performance at room temperature. Two dedicated ASIC chips have been developed for steering and readout of the pixel matrix. The measured system noise of $(69 \pm 4)\,e^-$ at 35 °C is mostly due to sensor leakage current and can be largely reduced by cooling or a faster readout. The spatial resolution is examined by measurements with a laser as well as with a dedicated test chart and is determined to be (6.7 ± 0.7) μm for 6 keV-X-rays and 4.3 ± 0.8 μm for 22 keV-X-rays. The measurements are compared to simulation results with different reconstruction algorithms. Due to the thin entrance window at the detector backside and the low noise performance, a detection of low-energy β-emitters such as ^{3}H is possible. Measurements with ^{3}H-labeled biological samples were taken. The ability of the DEPFET pixel Bioscope to separate different radiolabels in the same sample is demonstrated by a measurement with ^{3}H and ^{14}C.

*Corresponding author. Tel.: +49 6221 8935114.
E-mail address: johannes_ulrici@web.de (J. Ulrici).
[1]Now at Sirona Dental Systems GmbH, Fabrikstr. 31, 64625 Bensheim, Germany.
[2]Now at Universität Mannheim, Technische Informatik, D 7, 68159 Mannheim, Germany.
[3]Now at PRÜFER & PARTNER Patentanwälte GbR, Germany.
[4]Now at NEC Electronics (Europe) Gmbh, Kanzlerstr. 2, 40472 Düsseldorf, Germany.

1. Introduction

In recent years, great progress has been made in the development and operation of DEPFET (DEPleted Field Effect Transistor) pixel detectors [1–5]. In the DEPFET concept, the first amplifying transistor is integrated into every pixel cell of the sensor [6]. This leads to a small input capacitance and a reduction of stray capacitances due to connections between sensor and amplifier. A very low noise performance can thus be achieved. With DEPFET single pixels, an electronic noise of $\mathrm{ENC} = 4.8 \pm 0.1\, e^-$ has been measured [5], showing the low noise potential of the detector concept.

Possible applications of DEPFET pixel detectors in particle physics and X-ray astronomy experiments are presently being investigated. DEPFET pixels are one of the options [7–9] for the vertex detector at a e^+e^- linear collider as for example TESLA [10] (TeV Energy Superconducting Linear Accelerator) and [11] for the wide field imager at the XEUS (X-ray Evolving Universe Spectroscopy) satellite [12].

The DEPFET pixel Bioscope system, which is the subject of this paper, operates a 64×64-matrix of DEPFET pixels and was developed as a system for applications in time-, energy- and spatially resolved digital autoradiography. Due to the very thin entrance window of the DEPFET detector, the detection of low energy β-radiation such as ^{3}H is possible [4]. Additionally, the good energy resolution of the system allows the separation of different radiomarkers in the same sample.

In Sections 2 and 3, the DEPFET principle and the operation principle of a whole pixel matrix are explained. The readout electronics of the DEPFET pixel Bioscope system is described in Section 4. Section 5 deals with the noise performance of the system. The results of theoretical and experimental studies on the spatial resolution are presented in Section 6. Measurements with ^{3}H-labelled biological samples and the separation of different markers are covered by Sections 7 and 8.

2. Principle of DEPFET sensors

In the DEPFET pixel detector concept, the first amplifying transistor is integrated into the sensor itself (Fig. 1).

The transistor is realized as an annular p-channel JFET with the source in its center. The sensor material consists of a 300 μm-thick high resistivity n-silicon substrate, which is operated fully depleted. By sidewards depletion [13] and an additional n^+-implantation below the JFET, a potential minimum for electrons is created right underneath the transistor channel, which can be considered as an internal gate of the JFET. The backside of the device consists of a p^+-implant and a passivation layer which results in a 200 nm-thin entrance window allowing a low-energy radiation detection.

Radiation impinging from the detector backside creates electron–hole pairs. While the holes drift to the rear contact of the device, the electrons are collected and stored in the internal gate of the JFET. The resulting change in the internal gate potential leads to a modulation of the transistor current which can be measured.

The charge generated by leakage current and radiation fills up the internal gate and has thus to be removed from time to time. This can be accomplished by applying a positive voltage pulse to an additional n^+-contact outside of the transistor area (“clear” in Fig. 1). Another possible reset mechanism is the application of a positive voltage pulse to the external transistor gate, which

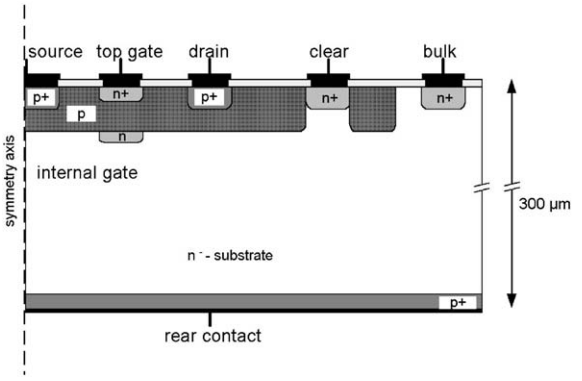

Fig. 1. Schematic cross-section of a DEPFET pixel half cell.

removes the charge by punch-through through the transistor channel. This simplifies the setup, since the clear contact does not need to be connected to the readout electronics.

It should be noted here that since the charge is stored in every pixel cell and the change in the transistor current is therefore stationary, a pixel does not need to be read out continuously. Due to this property, the number of readout channels can be significantly reduced, thus avoiding bump bonding and resulting in a small scale readout chip.

3. Operation of a DEPFET matrix

A section of a 64×64 matrix of hexagonal DEPFET pixels is shown in Fig. 2. The gate, source and clear contacts are connected row-wise to each other by aluminium traces and can be accessed on the sides of the matrix by wire-bonds. The drains of the transistors are connected column-wise by p^+-implantations and can be contacted at the bottom of the matrix.

If a sufficiently positive voltage is applied to the transistor gates, the transistor current is switched off. By switching off all but one row of the matrix and by reading out the transistor currents column-wise, the pixels in the matrix can be randomly accessed (Fig. 3).

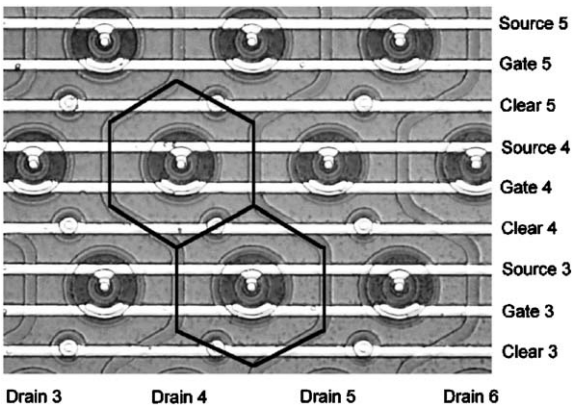

Fig. 2. Section of a matrix of hexagonal DEPFET pixels.

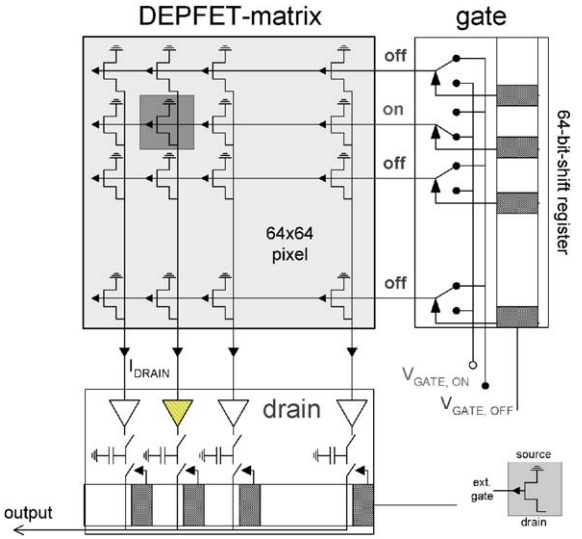

Fig. 3. Readout principle of DEPFET matrix. The clear contacts are not connected, since the matrix pixels are reset by applying a positive voltage pulse to the external gate.

The readout of one row i of the $n \times m$-matrix can now be envisaged as follows:

- The pixels of the row i are reset. For this detector this is accomplished by punch-through from the external to the internal gate.
- The pixels of the row i are switched on by changing the gate voltage, while the other rows of the matrix remain switched off. The n transistor currents of the pixels are read out in parallel at the drains, yielding the pedestal currents I_{Ped}.
- After a certain integration time Δt, the transistor currents are read out again, yielding the signal currents I_{Sig}.

The difference between the pedestal and the signal current $\Delta I = I_{\mathrm{Sig}} - I_{\mathrm{Ped}}$ is proportional to the amount of charge collected during Δt. The minimum integration time is given by the time needed to repeat the readout for the other 63 rows of the matrix. In the case of the DEPFET pixel Bioscope system, the resulting minimum integration time is 1.5 ms.

4. Readout electronics

The picture of a DEPFET hybrid ceramic with a 64×64-matrix in its center and two dedicated ASICs can be seen in Fig. 4. The size of the sensitive area is $3.2 \times 3.2\,\mathrm{mm}^2$. Radioactive samples can be placed on the backside of the detector.

The readout control chip SWITCHER is placed on the right-hand side of the matrix. This chip was fabricated in the AMS 2 µm high voltage CMOS process and has 64 outputs for the gates of the matrix rows. Four different voltages between 0 and 15 V can be applied to each of the outputs. The chip is able to switch on and off the matrix rows and to reset the matrix row-wise.

The readout chip CARLOS 2.0 can be seen in Fig. 4 on the bottom of the matrix. This chip was fabricated in the AMS 0.8 µm CMOS process and has 64 channels for a parallel low noise read out of the 64 columns of the DEPFET matrix.

A schematic diagram of the main blocks of this chip is shown in Fig. 5. The drain potentials of the DEPFET pixels are kept constant by regulated cascodes, consisting of the two p-FETs M_1 and M_2 in Fig. 6. The drain voltage is set to $V_{\mathrm{ref}} = V_{\mathrm{cc}} - V_{\mathrm{thr}}$ by transistor M_1 with V_{thr} being the transistor threshold voltage, while M_2 acts as the feedback transistor. The DEPFET current is converted into a voltage by a resistor. The voltages are then stored on a sampling capacitance. The resistor was realized as two equally-sized parallel transistors of the same gain (Fig. 6) with one of the transistors being in a diode configuration. The circuit has a much smaller size than a polysilicon

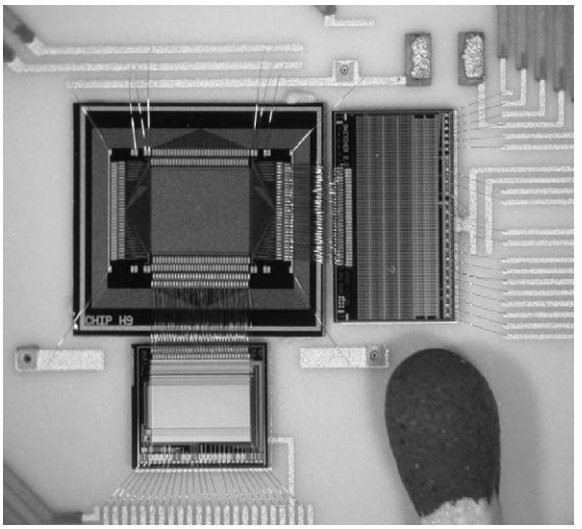

Fig. 4. DEPFET Pixel Bioscope system hybrid.

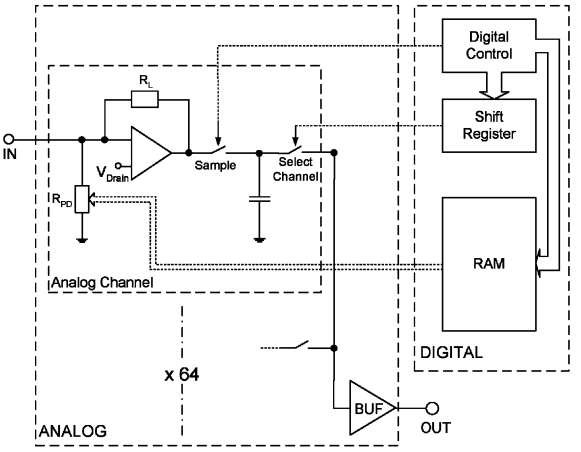

Fig. 5. Schematic of the readout chip CARLOS 2.0.

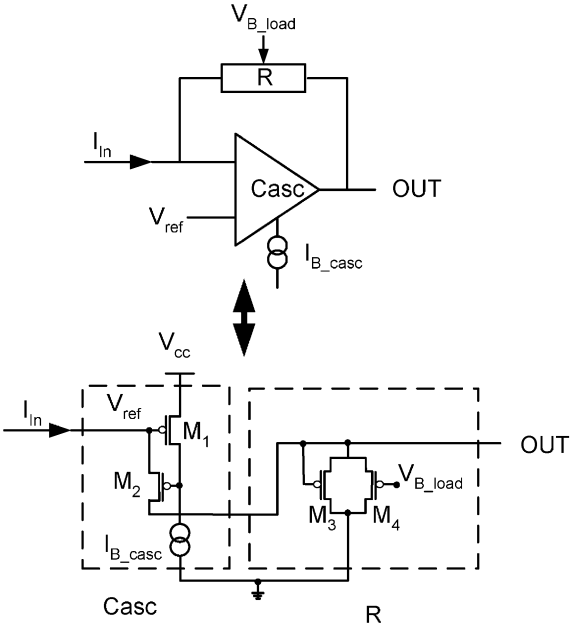

Fig. 6. Schematic of regulated cascode and load resistance for CARLOS 2.0.

resistor. For $V_{DS} \leqslant V_{GS} - V_{th}$, the I–V-characteristics of a transistor can be approximated by

$$I_{DS} = \frac{K_p}{2}\frac{W}{L}(2(V_{GS} - V_{th}) - V_{DS}^2), \quad (1)$$

where V_{GS} is the voltage between gate and source, V_{DS} the voltage between drain and source and V_{th} the threshold voltage of the transistor. K_p is the transconductance parameter given by the technology. As can be calculated from this equation, the quadratic parts of the I–V characteristics of diode and transistor cancel each other resulting in a linear output characteristics of the circuit in this region. A measurement of the output characteristics is shown in Fig. 7. The differential non-linearity of the circuit is $<3\%$ for voltages between 0 and 5 V and a gate voltage of $V_{B\_load} = 7\,V$. The non-linearities are corrected offline.

The stored signals of the 64 readout channels are demultiplexed to a fast readout buffer by a shift register.

Since the ratio of the DEPFET current contributions from offset current ($\sim 300\,\mu A$) and signal current ($<1\,\mu A$) is quite large, the offset current is subtracted before further amplification is performed in the readout chip. This allows to better exploit the dynamic amplification range for the signal part. Noise contributions which appear after the subtraction therefore influence less the SNR. The subtraction is accomplished by applying a voltage to a polysilicon resistor connected to the input node. Due to the DEPFET fabrication process, the offset current of all of the 4096 DEPFET pixels in a matrix varies up to 20% such that for each of the pixels an individual offset current has to be subtracted. This is accomplished by storing a 4-bit-value for each matrix pixel on an on-chip-RAM. This value is used to switch on and off resistor segments, thus changing its size and the amount of subtracted current.

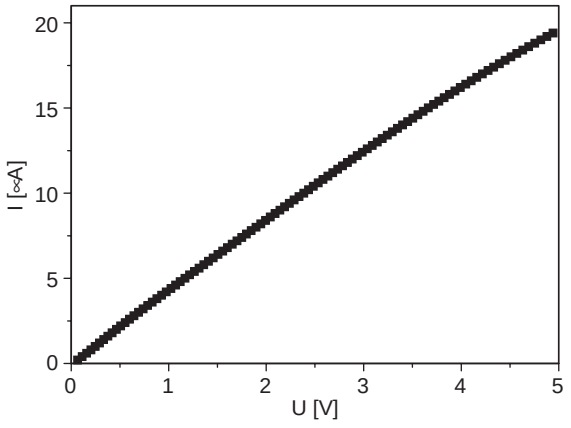

Fig. 7. Measured output characteristics of the load resistance of CARLOS 2.0. The gate voltage applied to transistor M_4 in Fig. 6 was $V_{B\_load} = 7\,V$.

The complete hybrid is built into the DEPFET pixel Bioscope system, which has been described earlier in detail [4].

5. Noise performance

The noise of a pixel in the matrix configuration was determined by calibrating the system with a radioactive source and measuring the width of the noise peak. A total system noise of ENC $= 114 \pm 6\,e^-$ was measured, the error being given by the incertainty of the energy calibration due to gain variations for the 4096 pixels of the matrix. The DEPFET transistors are operated in saturation. Since the gain of a JFET in saturation is roughly proportional to the square root of its current, the variation in gain is much smaller than the variation in transistor currents. The operating temperature was 45 °C due to the heating of the electronics. The noise is dominated by the sensor leakage current accumulated during the integration time of $\Delta t = 1.5\,ms$. The noise resulting from the measured leakage current can be calculated using the known equation [14]

$$ENC_{leak}^2 = q\,I_{leak}\,\Delta t. \quad (2)$$

As can be seen in Table 1, the noise calculated with this formula is $ENC_{leak} = 104\,e^-$, which is in good agreement with the measurement. Even by a gentle

Table 1
Noise of the DEPFET pixel Bioscope system

T	I_{leak}	Calculated ENC_{leak}	Measured ENC_{leak}
45 °C	1.15 pA/pixel	$104\,e^-$	$114 \pm 6\,e^-$
35 °C	0.34 pA/pixel	$56\,e^-$	$69 \pm 4\,e^-$

cooling of the system by $\Delta T \approx 10\,^{\circ}\mathrm{C}$ resulting in a hybrid temperature of $T = 35\,^{\circ}\mathrm{C}$, the system noise could be reduced to $\mathrm{ENC} = 69 \pm 4\,e^{-}$.

The intrinsic noise of the DEPFET detector has been determined earlier in measurements on single pixel devices. A noise of $\mathrm{ENC} = 4.8 \pm 0.1\,e^{-}$ was measured for a shaping time of 10 μs at room temperature [5]. A more aggressive cooling and a shorter integration time due to a faster readout are planned in future DEPFET projects, such that the system noise will be further reduced. No further cooling is desired for autoradiography applications, however, since an operation at room temperature is important.

6. Spatial resolution

Depending on the application, different definitions of the spatial resolution of a system are in use. While in particle detection the root mean square hit reconstruction error is used most often, this is not the most sensible term to describe the resolution properties of an imaging system, for which the ability to resolve structures is characterized by the highest resolvable spatial frequency.

6.1. Simulation studies

Simulations were carried out in order to study the spatial resolution of DEPFET pixels theoretically. Pixels with both quadratic (staggered in the y-direction) and hexagonal geometries were examined (Fig. 8).

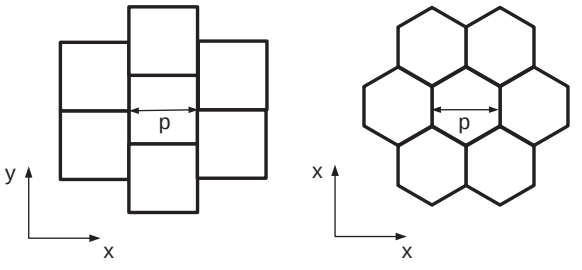

Fig. 8. Quadratic and hexagonal geometry of DEPFET pixel matrices ($p = 50\,\mu\mathrm{m}$).

The following procedure is repeated using high statistics event generation:

- The spatial position $\overrightarrow{r}$ of a particle entering the detector is chosen randomly. A point-like charge cloud at the detector backside is assumed, which is a good approximation for low-energy β- and γ-rays.
- The charge cloud broadens by diffusion while drifting to the detector front side, resulting in a gaussian shape of the cloud with width σ. Simulations with cloud sizes between 1 and 20 μm were carried through.
- The signal amplitude is calculated for the hit pixel as well as for its neighbors by two dimensional integration over the pixel area.
- Random noise is added to the signal using different values for the signal-to-noise-ratio SNR.
- The reconstructed hit position $\overrightarrow{r_{\mathrm{rec}}}$ is compared to the particle entrance position. The root mean square of the obtained error distribution is taken as the reconstruction error $\Delta r = \sqrt{\langle(\overrightarrow{r} - \overrightarrow{r_{\mathrm{rec}}})^2\rangle}$.

Three types of reconstruction algorithms are used. All of them make use of charge sharing between neighboring pixels:

- Linear interpolation between the two pixel columns and rows with the largest collected charge signal.
- The η-function algorithm [15]: The amount of charge sharing for an event can be described by the parameter $\eta = Q_1/(Q_1 + Q_2)$, Q_1 and Q_2 being the signal in the two rows or columns with the largest collected charge. The η-value distribution as detector response to a homogeneous irradiation is determined by a measurement. This distribution is used to construct a function which assigns a hit position to any given η. The advantage of this method is that the η-function can easily be determined by a measurement.
- Lookup table method: For any hit position, the charge collected by the hit pixel and by its neighbors is stored in a lookup table. For an event, the observed charge sharing of a pixel

cluster is then compared to the values stored in the lookup table, yielding the reconstructed position. To setup the necessary lookup table is experimentally difficult, since the hit position has to be known from a reference.

Note that the charge sharing between neighboring pixels in a hexagonal pixel geometry in the y-direction always depends on the x-position and vice versa. The reconstruction in both directions can therefore not be treated independently from each other, as is necessary for the linear interpolation or the η-function algorithms. For hexagonal pixels the lookup table method is therefore the most suited.

The only algorithm which returns a homogeneous image for a homogeneous input activity distribution is the η-function algorithm. This is due to the influence of noise on the reconstruction error, which depends on the position of the hit in the pixel. If a hit close to the pixel center occurs, almost no charge will be collected in the neighboring pixels. Noise in one of the neighboring pixels, however, shifts the reconstructed position to the pixel edge. This effect is smaller for hit positions near the pixel edges. A reconstruction with the η-function algorithm takes this into account by construction.

The typical development of the reconstruction error as a function of the width of the charge cloud is shown in Fig. 9 for a treatment using the η-function algorithm and different SNR values. The pixels have a quadratical and staggered geometry with a length of $p = 50\,\mu\text{m}$. For comparison, the error obtained with a simple binary readout given by $p/\sqrt{12}$ is also shown (dashed line). We conclude: (a) The higher the SNR the better is the reconstruction. (b) The reconstruction performance improves for larger charge clouds, since more charge sharing occurs and a better position interpolation is possible. For very large charge clouds, however, the resolution deteriorates again due to the charge being distributed between too many pixels leading to a higher influence of the noise. Thus, an optimum ratio σ/p for the spatial resolution exists. These results are also valid for the other reconstruction algorithms studied, as well as for the hexagonal pixel geometry.

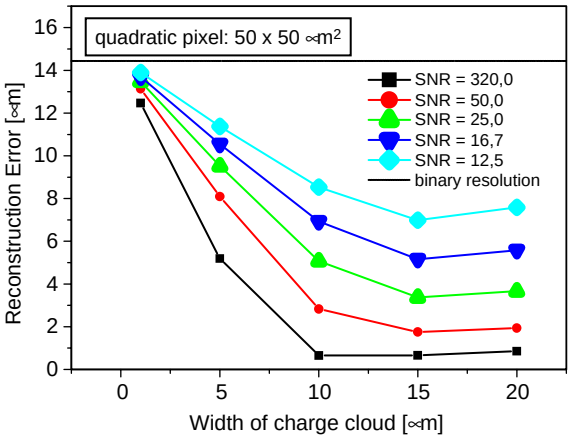

Fig. 9. Simulated spatial resolution for a quadratic staggered pixel geometry and for different SNR. The dashed line shows the spatial resolution for a simple binary readout, given by $p/\sqrt{12}$.

The most important results of the simulations shall be summarized here:

- For a quadratic pixel geometry, the reconstruction with a lookup table leads to the lowest reconstruction error. Compared to the reconstruction using the η-function algorithm, the difference in the reconstruction errors is less than 15%, a tolerable effect for most applications given that the η-function can be determined much more easily. In most of the cases studied, the reconstruction using a linear interpolation yields the worst results, as expected. For a high SNR (SNR $\geqslant$ 50) and a cloud size of 10 μm, e.g., the reconstruction error is almost twice as high as the one obtained using the η-function algorithm. For low SNR values, however, the results obtained by linear interpolation become comparable to the other algorithms.
- In most of the cases studied, the spatial resolution for a hexagonal pixel geometry was better than the one obtained for quadratic staggered pixels of the same area, although the difference for the two pixel geometries was very small ($<5\%$ in all of the cases). It should be noted, that for hexagonal pixels the resolution is equally good in the x- and the y-direction, while for quadratic pixels—due to the staggered

geometry—the resolution in the y-direction is better.

6.2. *Measurement of the reconstruction error*

To measure the mean square reconstruction error of the DEPFET pixel Bioscope system, a signal charge is deposited in the detector by applying a laser pulse. Since the position of the laser spot is known, the reconstructed position can be compared to the real position of the charge deposition. The procedure is repeated several times and for different positions of the laser spot in the DEPFET pixel, thus yielding the mean square reconstruction error. A lookup table can be obtained in a similar way.

In order to determine the size of the charge cloud, a laser scan in y-direction was carried out (Fig.10 left). In Fig.10 right, the measured signal amplitude of three adjacent pixels is shown. The derivative of this response function on the edge of a pixel yields the size of the charge cloud, which can be determined to be $\sigma = (12.0 \pm 0.2)\,\mu\text{m}$.

The measured mean square reconstruction error is listed in Table 2 for different signal-to-noise SNR and for different pixel geometries. The hit positions were reconstructed using a lookup-table. In order to compare the experimental results to theory, the measured SNR and the measured size σ of the charge cloud were used as input parameters for the simulation procedure described in Section 6.1. The simulated values for the reconstruction error are also listed in the table. The measured spatial resolution is in good agreement with the simulation results. For an SNR ≈ 30 and a square staggered pixel geometry, e.g., a mean square reconstruction error of $\Delta = 3.3\,\mu\text{m}$ is expected. The measured value was $\Delta = 2.7 \pm 0.7\,\mu\text{m}$ for a charge signal of $S = 3100\,e^-$.

Due to the size of the laser spot, the performed laser measurements can only be compared with caution to measurements using radiation from radioactive sources. By analyzing the amount of split events in an ^{55}Fe-spectrum the width of the charge cloud for the 6 keV-γ-radiation has been determined to about $\sigma \approx 8\,\mu\text{m}$. Using the above simulation studies, which agree well with the laser measurements for the measured SNR and σ, an estimate can be made of the achievable reconstruction error using β radiation from tritium decays which have a mean energy of 5.7 keV. With the measured system noise of ENC $= 114 \pm 6\,e^-$ the signal-to-noise ratio is SNR ≈ 14. Hence, a mean reconstruction error of $\sigma \approx 9.3\,\mu\text{m}$ can be expected for autoradiography using ^{3}H.

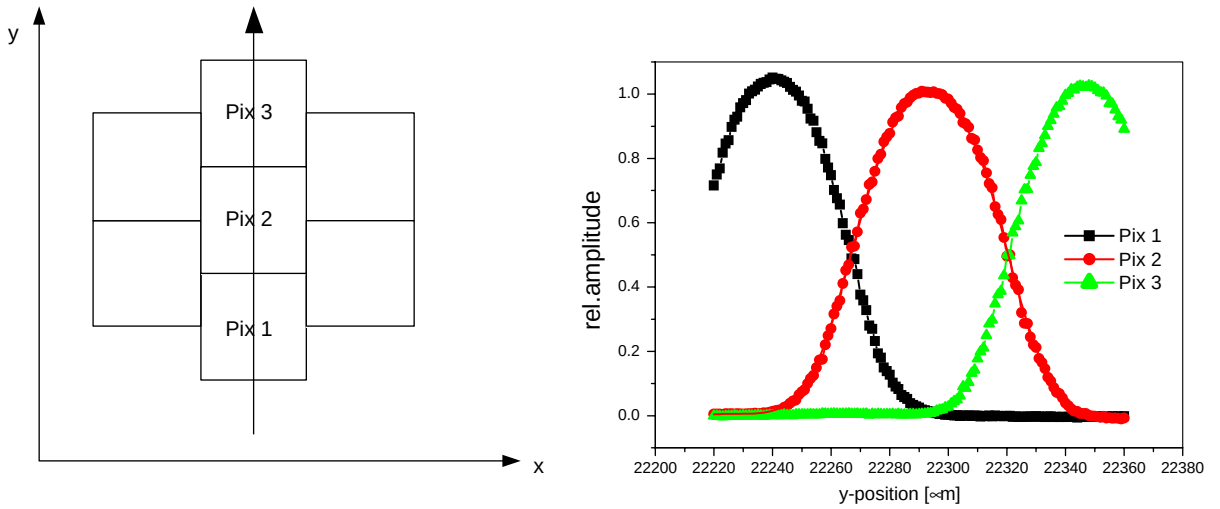

Fig. 10. Left: schematic of laser scan to determine the width of the charge cloud. Right: Response of three neighboring pixels on laser scan.

Table 2
Mean square reconstruction error of the DEPFET pixel bioscope system.

Geometry	p (μm)	Cloud size σ (μm)	SNR	Theoretical resolution (μm)	Measured resolution (μm)
Quad	50	12	30	3.3	2.7 ± 0.7
Quad	50	12	70	1.4	1.7 ± 0.3
Quad	50	8	14	9.3	—
Hex	50	12	30	2.7	3.2 ± 0.6

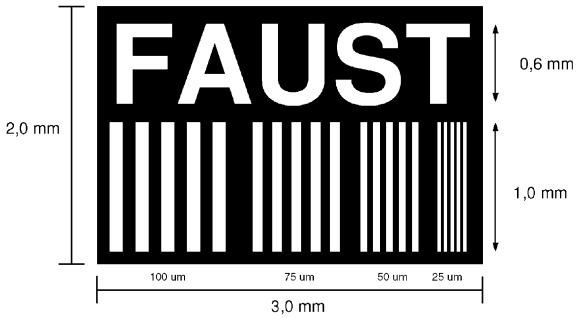

Fig. 11. Tungsten test chart as placed on the detector.

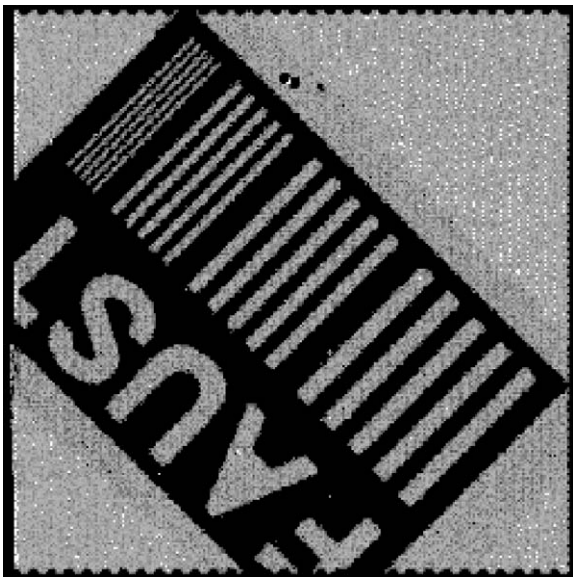

Fig. 12. ^{55}Fe shadow image of the test chart, reconstructed with the η-function algorithm.

6.3. *Measurements with a test structure*

Since the mean square reconstruction error does not adequately describe the capability of an imaging system to resolve structures, a $3 \times 2\,\mathrm{mm}^2$ tungsten test chart (Fig.11) was placed on the detector backside at an angle of 45° relative to the pixel orientation. It was then irradiated with a ^{55}Fe-source. The width of the lines as well as the spacing between them is 25, 50, 75 and 100 μm, respectively. The image reconstructed with the η-function algorithm is shown in Fig.12. Even the most narrow line pairs are clearly resolved in the image, as demonstrated in the projection in Fig. 13 left.

The intensity distribution close to the line edge is described by an error function. The spatial resolution of the system is hence given by the width of its derivative (Fig. 13 right). The spatial resolution is determined this way to $\sigma = 6.7 \pm 0.7\,\mu\mathrm{m}$ for 6 keV-γ-radiation. This corresponds to a resolution of $\mathrm{MTF}_{0.3} = 37 \pm 3\,\mathrm{LP/mm}$ at the 30%-point of the modulation transfer function MTF. This is in good agreement with theoretical results obtained by simulating the experiment, predicting a spatial resolution of $\sigma_{\mathrm{theor}} = 7.1 \pm 0.8\,\mu\mathrm{m}$. A spatial resolution of $4.3 \pm 0.8\,\mu\mathrm{m}$ or $\mathrm{MTF}_{0.3} = 57 \pm 10\,\mathrm{LP/mm}$, respectively, is obtained experimentally for 22 keV-γ-radiation.

Since the mean energy for ^{3}H-decays is 5.7 keV, a spatial resolution of ~7 μm is estimated for Tritium detection. This can be compared to the mean square reconstruction error of 9.3 μm determined in Section 6.2.

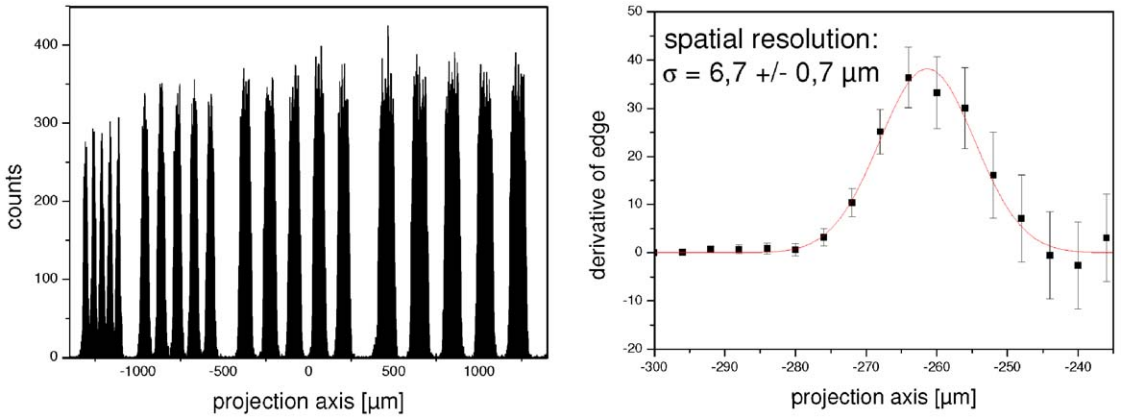

Fig. 13. Left: Projection of ^{55}Fe test chart shadow image to an axis perpendicular to the line pairs. Right: Derivative of the intensity distribution close to one of the line edges.

Fig. 14. Left: Leaf labelled with ^{3}H. The size of the leaf is $12 \times 11\,\mathrm{mm}^2$. Right: Autoradiogram of the leaf.

7. ^{3}H-measurements with biological samples

^{3}H is widely used as a radioactive tracer in biomedical applications. Because of its very short mean range of about 200 nm, however, its detection with silicon detectors is difficult. Measurements with a ^{3}H-microscale have been published earlier [4], proving that ^{3}H-decays can be detected with the DEPFET pixel Bioscope system. This is due to the very thin entrance window of 200 nm at the backside of the detector as well as to its low noise performance.

To demonstrate the ability of the system to measure ^{3}H-distributions in biological samples, a ^{3}H-labelled leaf (Fig. 14 left) was put on the detector backside. Because of the small size of the detector of only $3.2 \times 3.2\,\mathrm{mm}^2$, the leaf with a size of $12 \times 11\,\mathrm{mm}^2$ was cut into pieces before measuring the activity distribution. In Fig. 14 right, the autoradiogram obtained after 2 h of exposition is shown. The shape of the leaf can clearly be seen in the image, the highest activity being measured at its edges, where most of the transpiration takes place.

8. Spatial separation of different markers

Due to the very good energy resolution of the DEPFET pixel Bioscope system, different radiolabels can be separated in the same sample. This has been demonstrated by placing a ^{14}C-labelled twine together with a piece of a ^{3}H-labelled leaf on the detector (Fig. 16a). ^{3}H-decays have a mean energy of 5.7 keV and an endpoint energy of 18.6 keV, while ^{14}C-decays have a mean energy of 49.5 keV and an endpoint energy of 240 keV. The energy distribution for both sources as measured with the system is shown in Fig. 15.

If only hit, but no energy information is used the twine and the leaf cannot be separated from each other (Fig. 16 b). They can be individually imaged, however, by cutting in the measured energy distribution. Requiring at least $E = 20$ keV, the resulting hits are due to ^{14}C-decays only and the twine is emphasized in the image (Fig. 16c). In order to image the ^{3}H-labelled leaf the expected number of ^{14}C-decays with energies smaller than 20 keV is calculated for every pixel of the matrix using the measured number of ^{14}C-decays with energies larger than 20 keV in this pixel and the known ^{14}C energy distribution. Subtracting these decays from the total number of low energy decays yields the number of ^{3}H-decays. The ^{3}H-labelled leaf is thus clearly seen in Fig. 16d. This demonstrates the capability of the DEPFET pixel Bioscope system to separate different, low energy radiolabels in the same sample.

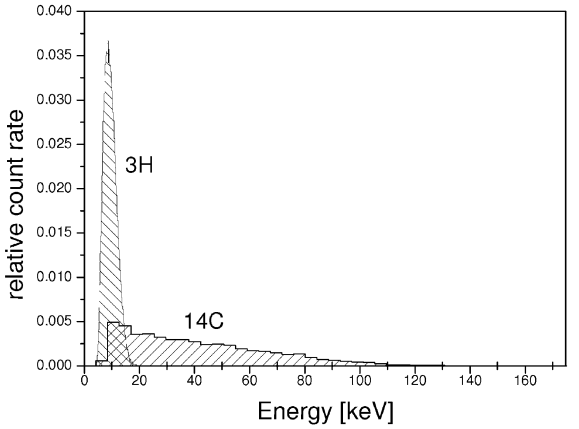

Fig. 15. Measured energy distribution for ^{3}H and ^{14}C.

9. Summary

The DEPFET pixel Bioscope system has been designed as a prototype system for autoradiography in biomedical applications. In order to operate a full matrix of 4096 DEPFET pixels the readout electronics including two dedicated ASICs has been developed in our group. Since in the internal gate of DEPFET pixels the charge is stored until readout, a readout concept was realized which avoids expensive bump bonding as well as a large scale readout chip.

A system noise of ENC $= 114\,e^{-}$ has been determined, which is still good in comparison to other pixel detectors, although worse than for single isolated DEPFET pixels. This is due to the long integration time when reading out the full DEPFET matrix row by row, which results in a higher leakage current. This noise contribution is significantly reduced simply by cooling.

The spatial resolution of the DEPFET pixel Bioscope system was studied theoretically as well as experimentally by measurements with a laser and with radioactive sources. For ^{55}Fe-decays, a spatial resolution of $6.7 \pm 0.7\,\mu$m or MTF$_{0.3} = 37 \pm 3$ LP/mm was measured. A spatial resolution of $4.7 \pm 0.8\,\mu$m or MTF$_{0.3} = 57 \pm 10$ LP/mm was determined for ^{109}Cd-decays. For Tritium, a spatial resolution of $\sim 7\,\mu$m can thus be inferred.

It has been shown that a ^{3}H-distribution in a biological sample can be measured with the system. Different radiolabels can be separated in the same sample due to the very good energy resolution, which was proven on the example of ^{3}H and ^{14}C.

These results demonstrate that DEPFET pixel detectors are well suited for certain demanding applications in digital autoradiography, where good energy and spatial resolution is needed at the same time. The greatest drawback at the moment is the small detector size of 3.2×3.2 mm. This will be overcome in the near future with the operation of much larger matrices.

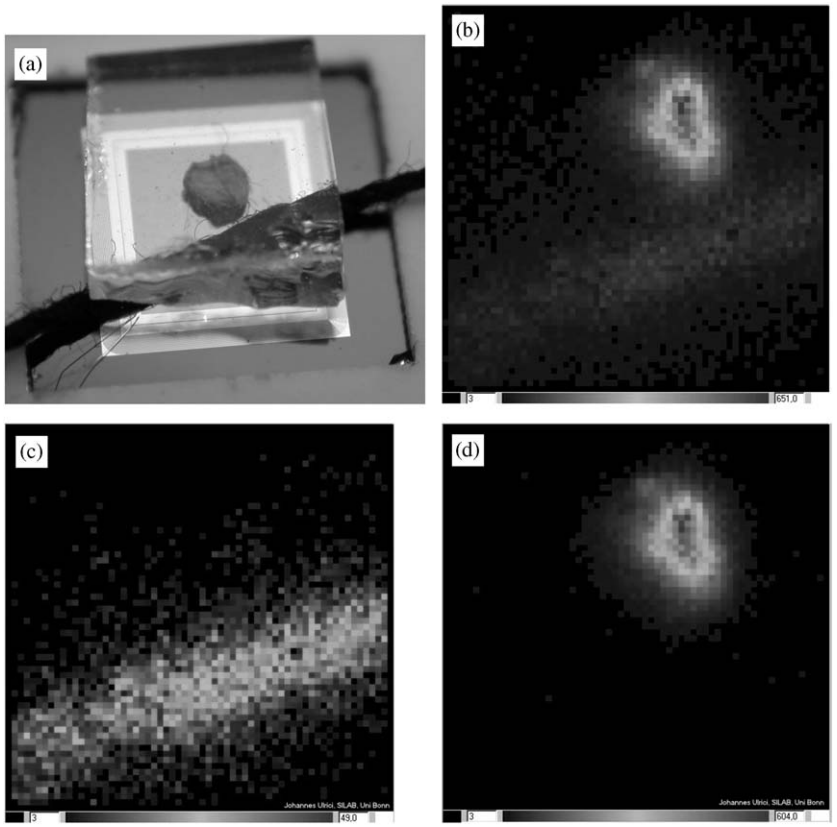

Fig. 16. (a) Simultaneous measurement of ^{3}H- and ^{14}C-decays with a piece of a ^{3}H-labelled leaf and a ^{14}C-labelled twine. (b) Hit distribution if no energy information is used. (c) Hit distribution for ^{14}C-events. The twine but not the leaf is seen in the image. (d) Hit distribution for ^{3}H-events. The leaf but not the twine is seen in the image.

Acknowledgements

The authors would like to thank Walter Ockenfels and Dr. Oegmundur Runolfssen for wire bonding, Prof. Dr. Ruprecht Schmidt for the preparation of the biological samples and Dieter Gebauer for the fabrication of the DEPFET Hybrids.

References

[1] G. Cesura, N. Findeis, D. Hauff, N. Hörnel, J. Kemmer, P. Klein, P. Lechner, G. Lutz, R.H. Richter, H. Seitz, New pixel detector concepts based on junction field effect transistors on high resistivity silicon, Nucl. Instr. and Meth. A 377 (1996) 521.

[2] P. Fischer, J. Kemmer, P. Klein, M. Löcker, G. Lutz, W. Neeser, L. Strüder, N. Wermes, First operation of a pixel imaging matrix based on DEPFET pixels, Nucl. Instr. and Meth. A 451 (2000) 651.

[3] W. Neeser, M. Böcker, P. Buchholz, P. Fischer, P. Holl, P. Klein, H. Koch, M. Löcker, G. Lutz, H. Matthäy, L. Strüder, M. Trimpl, J. Ulrici, N. Wermes, DEPFET—a pixel device with integrated amplification, Nucl. Instr. and Meth. A 477 (2002) 129.

[4] W. Neeser, M. Böcker, P. Buchholz, P. Fischer, P. Holl, J. Kemmer, P. Klein, H. Koch, M. Löcker, G. Lutz, H. Matthäy, L. Strüder, M. Trimpl, J. Ulrici, N. Wermes, The DEPFET Pixel BIOSCOPE, IEEE Trans. on Nucl. Sci. NS-47 (3) (2000) 1246.

[5] J. Ulrici, S. Adler, P. Buchholz, P. Fischer, P. Klein, M. Löcker, G. Lutz, W. Neeser, L. Strüder, M. Trimpl, N. Wermes, Spectroscopic and imaging performance of DEPFET pixel sensors, Nucl. Instr. and Meth. A 465 (2001) 247.

[6] J. Kemmer, G. Lutz, New semiconductor detector concepts, Nucl. Instr. and Meth. A 253 (1987) 365.

[7] P. Fischer, W. Neeser, M. Trimpl, J. Ulrici, N. Wermes, A DEPFET based pixel vertex detector for the

detector at TESLA, Linear Collider Note, LC-DET-2000-004 (2002).
[8] M. Trimpl, L. Andricek, P. Fischer, G. Lutz, R.H. Richter, L. Strüder, J. Ulrici, N. Wermes, A fast readout using switched current techniques for a DEPFET-pixel vertex detector at TESLA, Nucl. Instr. and Meth. A 511 (2003) 257.
[9] R. Richter, L. Andricek, P. Fischer, K. Heinzinger, P. Lechner, G. Lutz, I. Peric, M. Reiche, G. Schaller, M. Schnecke, F. Schopper, H. Soltau, L. Strüder, J. Treis, M. Trimpl, J. Ulrici, N. Wermes, Design and technology of DEPFET pixel sensors for linear collider applications, Nucl. Instr. and Meth. A 511 (2003) 250.
[10] http://tesla.desy.de.
[11] P. Holl, P. Fischer, P. Klein, G. Lutz, W. Neeser, L. Strüder, N. Wermes, Active pixel matrix for X-ray satellite missions, IEEE Trans. Nucl. Sci. NS-47 (4) (2000).
[12] http://astro.estec.esa.nl/XEUS.
[13] E. Gatti, P. Rehak, Semiconductor drift chamber—an application of a novel charge transport scheme, Nucl. Instr. and Meth. A 225 (1984) 608.
[14] G. Lutz, Semiconductor Radiation Detectors, Springer, Berlin, 1999.
[15] R. Turchetta, Spatial resolution of silicon microstrip detectors, Nucl. Instr. and Meth. A 335 (1993) 44.